Plasmonics (2025) 20:11181–11192
https://doi.org/10.1007/s11468-025-03225-8

RESEARCH

Surface Plasmon Resonance Dual-Channel H-shaped Fiber Sensor for Simultaneous Detection of Refractive Index and Temperature

Zhenshi Chen[1] · Chengkun Yang[2] · Haihao Fu[3] · Paul K. Chu[4]

Received: 25 June 2025 / Accepted: 15 July 2025 / Published online: 18 July 2025

Abstract

A dual-channel H-shape fiber (DCHF) sensor inlaid with a notched capillary is designed for the simultaneous detection of refractive index and temperature. The DCHF is fabricated by symmetrically etching two rectangular grooves on both sides of a multimode fiber (MMF) with a femtosecond laser and then embedding the DCHF into a notched capillary. By filling the analyte and thermo-sensitive liquid into the two rectangular grooves, a DCHF-based dual-parameter sensor is constructed for synchronous detection of the refractive index of the analyte as well as temperature. Furthermore, the Al wires are modified at positions closest to the core in both rectangular grooves to excite surface plasmon resonance (SPR) to enhance the sensitivity. The structural parameters of the DCHF-based dual-parameter sensor are systematically and comprehensively optimized to achieve superior sensing performance. Simulation results demonstrate that the sensor can synchronously detect refractive indexes in the range between 1.30 and 1.39 and temperature between 20 °C and 60 °C. The maximum refractive index sensitivity of 8,400 nm/RIU and maximum temperature sensitivity of 37.6 nm/°C represent a significant improvement over those of previously reported devices. Owing to the ease of analyte filling, non-interfering channels, high sensitivity, and simple fabrication process, the DCHF-based dual-parameter sensor has enormous potential in biochemical analysis, environmental monitoring, and other applications.

Keywords Dual-channel sensing · Refractive index · Temperature · Surface plasmon resonance · Optical fiber sensor

Introduction

The refractive index is a fundamental property of matter [1]. In recent years, optical fiber refractive index sensors have attracted extensive attention in fields such as chemical analysis, biomedicine, and environmental monitoring due to their advantages of compact size, high sensitivity, and strong anti-electromagnetic interference capability [2, 3]. Traditional optical fiber refractive index sensors are primarily of the interferometric type. However, interferometric fiber sensors often suffer from complex optical paths, significant measurement errors caused by slight environmental perturbations, and complicated signal demodulation [4]. Therefore, the evanescent wave optical fiber refractive index sensor has gradually caught the attention of researchers on account of the simple fabrication and convenient signal demodulation [5]. Nevertheless, evanescent wave optical fiber refractive index sensors typically exhibit low sensitivity because of the limited penetration depth of evanescent waves and their weak interactions with surrounding media. To enhance the sensitivity, fiber sensors exploiting the surface plasmon resonance (SPR) effect [6, 7] have garnered widespread attention.

Optical fiber SPR refractive index sensors are common in fields such as food safety detection, biochemical analysis, and medical hygiene. In these applications, the refractive index of analytes is highly sensitive to the temperature. To overcome the cross-sensitivity of temperature and

✉ Chengkun Yang
yangck@zjlab.ac.cn

1 School of Electronic Information, Huzhou College, Huzhou 313000, People's Republic of China

2 ZhangJiang Laboratory, Shanghai 201210, China

3 Key Laboratory of Communication and Information Systems, Beijing Municipal Commission of Education, School of Electronic and Information Engineering, Beijing Jiaotong University, Beijing 100044, China

4 Department of Physics, Department of Materials Science and Engineering, and Department of Biomedical Engineering, City University of Hong Kong, Tat Chee Avenue, Kowloon, Hong Kong, China

simultaneously monitor temperature variations, the fiber Bragg grating temperature sensor has been proposed [8]. Although this device achieves dual-parameter detection of the refractive index of the analyte and temperature, the sensing hardware is quite complex, making it very difficult to integrate the capability of refractive index and temperature detection by the same sensor. In this respect, photonic crystal fibers (PCFs) [9–11], which contain numerous air holes in the cladding, provide natural channels to fill the analyte. Additionally, the metal on the special air holes can excite SPR to improve the sensitivity. I. Danlard et al. have proposed a dual-polarization quasi-D-shape PCF-SPR sensor for simultaneous detection of refractive indexes from 1.35 to 1.46 and temperature from − 50 °C to 50 °C with maximum refractive index sensitivity and maximum temperature sensitivity of 5,000 nm/RIU and 3.0 nm/°C, respectively [12]. This sensor requires the deposition of Au films onto the inner walls of four air holes and filling them with liquid toluene. However, precisely filling toluene into the air holes while ensuring that it does not enter other air holes is quite difficult, especially due to the capillary effect arising from the similar diameter of the air holes requiring toluene filling and other air holes. To address this problem, A. Chen et al. have proposed a D-shape PCF-SPR sensor for simultaneous detection of the liquid refractive index and temperature [13]. In this device, ethanol is placed in the elliptical air hole of the sensor to sense the temperature, while the major and minor axes of the elliptical air hole guide the filling of the thermo-sensitive medium in specific directions to reduce the difficulty of ethanol filling. Nonetheless, the temperature sensitivity of only 1.075 nm/°C cannot satisfy the growing demand for temperature detection. J. Zhang et al. have designed an eccentric-core PCF-SPR dual-parameter sensor for simultaneous refractive index and temperature detection [14]. This sensor improves the temperature sensitivity by using thermo-sensitive liquid for temperature sensing, resulting in a maximum temperature sensitivity of 4.83 nm/°C in the temperature range from 20 °C to 60 °C. However, this sensor again requires depositing Au films onto the inner wall of the central air hole thus making it difficult to accomplish non-interference between the chemical reagent and thermo-sensitive liquid. Hence, in spite of these recent advances, it is still a significant challenge to design a highly integrated dual-parameter fiber sensor with a relatively simple structure, easy and non-interfering analyte filling, and easy fabrication.

In this work, a dual-channel H-shape fiber (DCHF) sensor inlaid in a notched capillary is designed for the simultaneous detection of analyte refractive index and temperature. The DCHF is fabricated by symmetrically creating rectangular grooves on both sides of the Ge-doped core with a femtosecond laser and embedding it into a notched capillary. When the DCHF is embedded into the notched capillary, two natural sensing channels are formed. By filling the analyte and thermo-sensitive medium into the two channels, synchronous detection of refractive index and temperature can be achieved. Meanwhile, two Al wires with different diameters are modified at positions closest to the core in the rectangular grooves to excite SPR to enhance the sensitivity. Systematic and comprehensive optimization of the DCHF dual-parameter sensor by the finite element method validates the superior refractive index and temperature ranges of 1.30–1.39 and 20 °C-60 °C and reveals a maximum refractive index sensitivity of 8,400 nm/RIU and maximum temperature sensitivity of 37.6 nm/°C, which are better than those reported recently by more than one order of magnitude [12–14, 25]. The DCHF-based dual-parameter sensor, which boasts advantages such as high integration, ease of analyte filling, and high sensitivity, has enormous potential in chemical production monitoring, biomedicine, and other areas.

Sensor Structure and Principle

To simplify the sensor structure, reduce the difficulty in filling the analyte, and enhance the refractive index sensitivity and temperature sensitivity, a DCHF-based dual-parameter sensor is inlaid in a notched capillary, as shown in Fig. 1. The diameter of the Ge-doped core is $\boldsymbol{d_0}$, and the relative refractive index difference between the core and cladding is $\boldsymbol{\Delta}$. The diameters of the two Al wires are $\boldsymbol{dm_1}$ and $\boldsymbol{dm_2}$, and the distances between the core and Al wires are $\boldsymbol{L_1}$ and $\boldsymbol{L_2}$ respectively. The radius of MMF is $\boldsymbol{R}$, and the thickness of the notched capillary is $\boldsymbol{t}$. The size of rectangular grooves is adjustable in order to reduce the difficulty in filling the thermo-sensitive liquid. In fact, filling a liquid analyte into the sensing channels near the notch of the capillary enables repeated detection of analytes with different refractive indexes.

The cladding of the DCHF sensor is made of SiO_2 and its refractive index is determined by the Sellmeier equation [15]. The refractive index of the Ge-doped core is slightly higher and can be obtained by Eq. (1) [16]:

$$\Delta = \frac{n_{core}^2 - n_{cladding}^2}{2n_{core}^2} \tag{1}$$

where $\boldsymbol{\Delta}$ is the relative refractive index difference between the core and cladding, and n_{core} and $n_{cladding}$ are the refractive index of the core and cladding, respectively. In the figure, the pink region represents the temperature-sensing channel filled with a thermo-sensitive liquid. The primary constituent of the thermo-sensitive liquid is chloroform, and its refractive index can be obtained with Eq. (2) [17]. In order to prevent chloroform from reacting with oxygen to form phosgene,

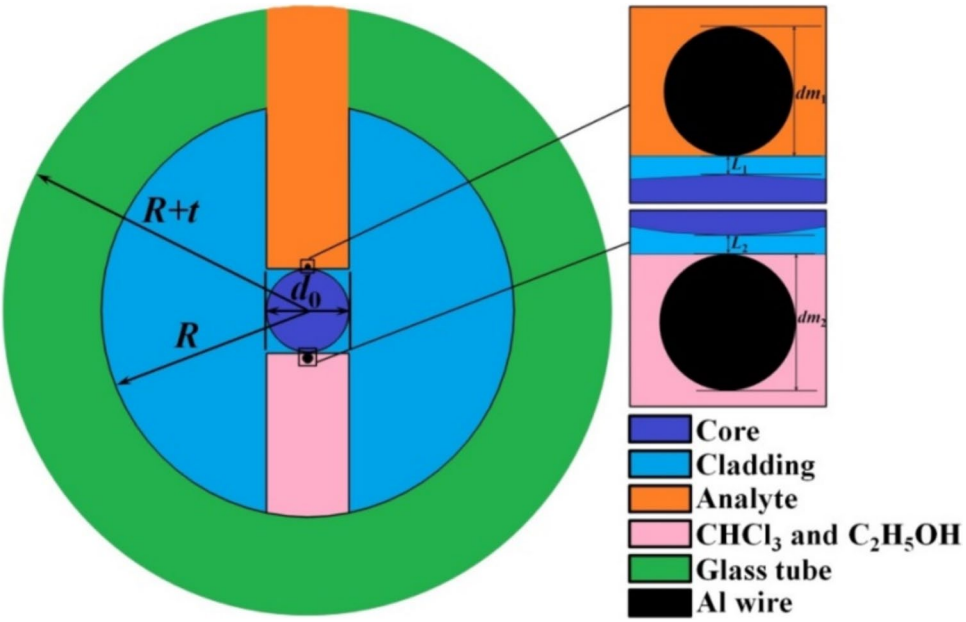

Fig. 1 Cross-section of the dual-parameter sensor with the DCHF inlaid in a notched capillary

0.6% ethanol is added to maintain the liquid phase. The refractive index of ethanol n_{Eth} can be by Eq. (3) [18]:

$$n_{Chl} = n_{Chl0} + \frac{dn_{Chl}}{dT}(T - 20) \tag{2}$$

$$n_{Eth} = n_{Eth0} + \frac{dn_{Eth}}{dT}(T - 20) \tag{3}$$

where $\boldsymbol{T}$ is the temperature, $dn_{Chl}/dT = -6.328 \times 10^{-4}$/℃ and $dn_{Eth}/dT = -3.94 \times 10^{-4}$/℃ are the thermo-optical coefficients of chloroform and ethanol respectively, and n_{Chl0} and n_{Eth0} are the refractive indexes of chloroform and ethanol at room temperature, which are determined by Eqs. (4) and (5) [19]:

$$n_{Chl0} = \sqrt{1 + \frac{1.04647\lambda^2}{\lambda^2 - 0.01048} + \frac{0.00345\lambda^2}{\lambda^2 - 0.15207}} \tag{4}$$

$$n_{Eth0} = \sqrt{1 + \frac{0.83189\lambda^2}{\lambda^2 - 0.00930} - \frac{0.15582\lambda^2}{\lambda^2 + 49.4520}} \tag{5}$$

where λ is the wavelength. The refractive index n_{mix} of the thermo-sensitive liquid can be calculated by Eq. (6) [19]:

$$n_{mix} = An_{Eth} + (1 - A)n_{Chl} \tag{6}$$

where $A = 0.6\%$ and $(1\text{-}A) = 99.4\%$ are the proportion of ethanol and chloroform in the thermo-sensitive liquid respectively.

The orange region is filled with the analyte, and the green region is the notched capillary, whose refractive index matches the cladding of DCHF. Although most metals can excite SPR, Al is chosen here to enhance the sensitivity because of the significantly larger real part of the relative dielectric constant compared to those of Au, Ag, and Cu, consequently facilitating energy conversion between the core and metal surface. The Al wires in both sensing channels of the DCHF-based dual-parameter sensor are sealed with the thermo-sensitive liquid and analyte to isolate them from air exposure and reduce oxidation. The relative dielectric constant of Al is obtained by Eq. (7) [20]:

$$\varepsilon_{Al}(\lambda) = 1 - \frac{\lambda^2\lambda_c}{\lambda_p^2(\lambda_c + i\lambda)} \tag{7}$$

where $\boldsymbol{\lambda_c} = 24.511$ μm and $\boldsymbol{\lambda_p} = 0.10657$ μm are the collision wavelength and plasma wavelength of Al and λ is the light wavelength in vacuum.

When light propagates in the Ge-doped core, an evanescent wave [21] is generated at the core-cladding interface when $n_{core} > n_{cladding}$. Additionally, collective oscillations of electrons occur when light arrives at the surface of Al wire and interacts with free electrons to generate a surface plasmon wave (SPW) [22]. When the propagation constants of the evanescent wave and SPW are the same, the phase-matching condition shown in Eq. (8) [23] is satisfied. At this point, a large amount of energy of the fundamental mode (FM) in the core is coupled with surface plasmon polariton (SPP) mode near the Al wires to produce a sharp increase of FM loss, which is calculated by Eq. (9) [24]:

$$K_{eva} = \frac{2\pi}{\lambda} n_{core} \sin\theta_i = \mathrm{Re}\left(\frac{2\pi}{\lambda}\sqrt{\frac{\varepsilon_{Al} n_{medium}^2}{\varepsilon_{Al} + n_{medium}^2}}\right) = K_{SPW} \tag{8}$$

$$Loss = \frac{2\pi}{\lambda}\frac{20}{\ln(10)}\mathrm{Im}\left(n_{eff}\right) \quad (9)$$

where θ_i is the incident angle of the incident light, n_{medium} is the refractive index of the analyte or thermo-sensitive liquid, K_{eva} and K_{SPW} are the propagation constants of evanescent wave and SPW respectively, and Im(n_{eff}) is the real part of the effective refractive index of FM.

The initial structural parameters of the DCHF-based dual-parameter sensor are $\boldsymbol{d_0}=35.0$ μm, $\boldsymbol{\Delta}=0.50\%$, $\boldsymbol{dm_1}=2.0$ μm, $\boldsymbol{dm_2}=3.1$ μm, $\boldsymbol{L_1}=0.5$ μm, $\boldsymbol{L_2}=0.5$ μm, $\boldsymbol{R}=32.5$ μm and $\boldsymbol{t}=15.0$ μm. When $\boldsymbol{n_a}=1.38$ and $\boldsymbol{T}=20$℃, the effective refractive index curves of FM and SPP mode and the loss spectrum of FM are shown in Fig. 2(a). Owing to the significant difference in refractive indexes between the analyte and thermo-sensitive liquid under identical conditions, the propagation constants of SPWs in the two sensing channels are disparate. Consequently, the refractive index curves of the FM and SPP mode intersect at 820 nm and 1,228 nm, respectively, indicating that the phase matching conditions are satisfied at the two wavelengths and causing continuous energy transfer from the FM to the SPP mode and larger FM loss. The field distributions of the FM and SPP modes in Fig. 2 demonstrate the effects. Concurrently, two loss peaks appear at 820 nm and 1,228 nm, named Peak 1 and Peak 2, and the wavelengths at the maximum FM loss are defined as the resonance wavelengths (RWs). Figure 2(b) shows that Peak 1 shifts toward longer wavelengths as $\boldsymbol{n_a}$ increases when the temperature is constant, while Peak 2 is fixed. This is because only Peak 1 is sensitive to the variation of $\boldsymbol{n_a}$. Similarly, Fig. 2(c) shows that as $\boldsymbol{T}$ increases, Peak 2 blueshifts while Peak 1 remains constant, confirming that only Peak 2 responds to temperature changes. Therefore, Peak 1 and Peak 2 can be utilized to detect $\boldsymbol{n_a}$ and $\boldsymbol{T}$ respectively. When $\boldsymbol{n_a}$ changes, the corresponding RWs of Peak 1 and Peak 2 are defined as RW_{1RI} and RW_{2RI}. If $\boldsymbol{T}$ changes, RWs are defined as RW_{1T} and RW_{2T}. Moreover, the four RWs display different degrees of deviation with changing $\boldsymbol{n_a}$ and $\boldsymbol{T}$. Hence, by monitoring the alteration of RW_{1RI} and RW_{2RI} with $\boldsymbol{n_a}$ as well as RW_{1T} and RW_{2T} with $\boldsymbol{T}$, simultaneous detection of $\boldsymbol{n_a}$ and $\boldsymbol{T}$ can be achieved.

Sensor Optimization

The characteristics of the DCHF-based dual-parameter sensor are affected by the diameter of the Ge-doped core, the relative refractive index difference between the core and the cladding, the diameter of the Al wires, and the distance between the Al wires and the core. Therefore,

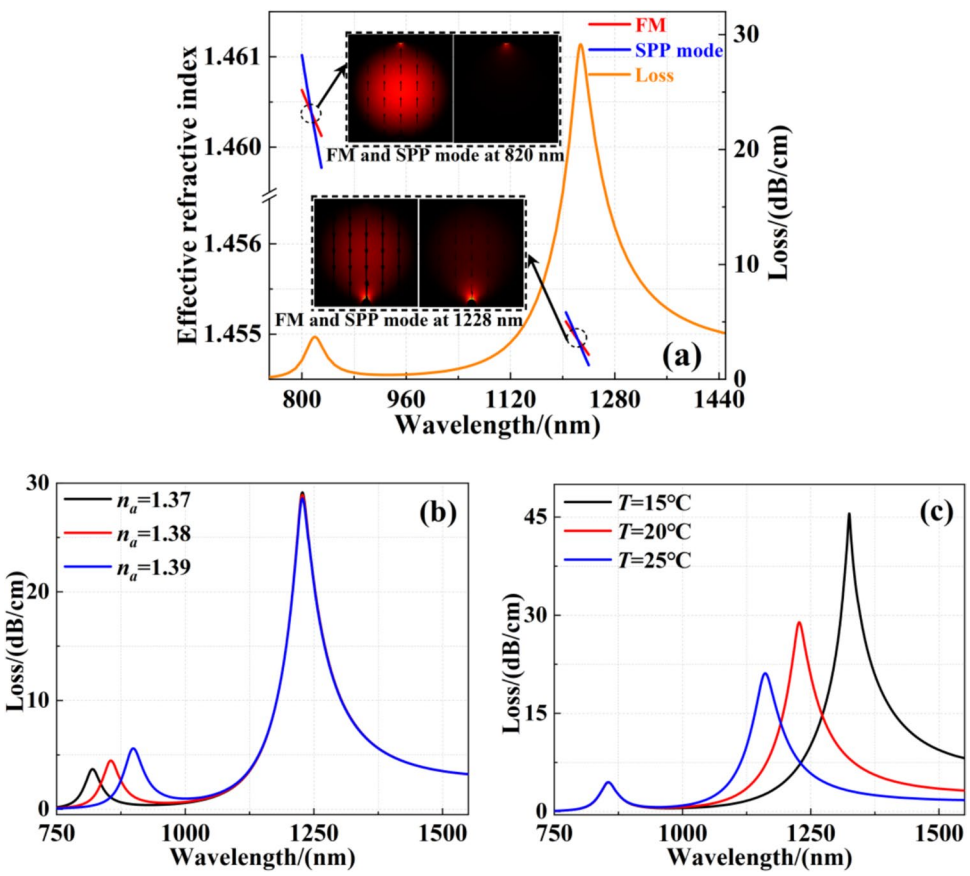

Fig. 2 (**a**) Effective indexes of the FM (red line) and SPP mode (blue line), and the loss spectrum of FM (origin line) with the insets showing the field distributions of the FM and SPP modes at 820 nm and 1,228 nm; (**b**) Loss spectra of FM for different $\boldsymbol{n_a}$ when $\boldsymbol{T}=20$℃; (**c**) FM loss curves for different $\boldsymbol{T}$ when $\boldsymbol{n_a}=1.38$

systematic and comprehensive optimization of these structural parameters is carried out. The refractive index sensitivity $S_1(RI)$ and temperature sensitivity $S_2(T)$ are selected as the optimization benchmarks, and the full-width at half-maximum (FWHM) and peak loss are also considered simultaneously. The initial structural parameters of the DCHF-based dual-parameter sensor are $\boldsymbol{d_0}=35.0$ μm, $\boldsymbol{\Delta}=0.50\%$, $\boldsymbol{dm_1}=2.0$ μm, $\boldsymbol{dm_2}=3.1$ μm, $\boldsymbol{L_1}=0.5$ μm, $\boldsymbol{L_2}=0.5$ μm, $\boldsymbol{R}=32.5$ μm, $\boldsymbol{t}=15.0$ μm, and the corresponding sensitivities are $S_1(RI)=4700$ nm/RIU and $S_2(T)=10.4$ nm/℃, respectively.

DCHF Core

As the primary medium for light conduction, the core of the DCHF is optimized first. The initial parameter of the $\boldsymbol{d_0}$ is 35.0 μm, and the optimization range is 20 μm $\leq \boldsymbol{d_0} \leq$ 40 μm. Figures 3(a)-(e) present the loss spectra of the FM for different $\boldsymbol{d_0}$, and the $S_1(RI)$ and $S_2(T)$ at $\boldsymbol{n_a}=1.38$ and $\boldsymbol{T}=20$℃ are summarized in Fig. 3(f). Since Peak 1 redshifts with increasing $\boldsymbol{n_a}$ and Peak 2 blueshifts with rising $\boldsymbol{T}$, a small distance between the two peaks will narrow the refractive index detection range and temperature detection range. When $\boldsymbol{d_0}=20.0$ μm and $\boldsymbol{d_0}=35.0$ μm, the distance between the two loss peaks is too small, so $\boldsymbol{d_0}$ should not be set to 20.0 μm or 35.0 μm. In addition, Fig. 3(f) indicates that both $S_1(RI)$ and $S_2(T)$ reach the maximum when $\boldsymbol{d_0}=25.0$ μm. Therefore, it is more appropriate to set $\boldsymbol{d_0}$ to 25.0 μm, while the corresponding $S_1(RI)$ and $S_2(T)$ are 5,100 nm/RIU and 14.2 nm/°C, respectively.

Based on $\boldsymbol{d_0}=25.0$ μm, the relative refractive index difference $\boldsymbol{\Delta}$ between the Ge-doped core and the cladding is further optimized with the initial $\boldsymbol{\Delta}=0.50\%$. When $\boldsymbol{\Delta}$ is increased to 0.55%, both $S_1(RI)$ and $S_2(T)$ decrease, so $\boldsymbol{\Delta}$ should be reduced. When $\boldsymbol{\Delta}<0.40\%$, a large amount of photon energy leaks from the core to the cladding, and therefore, $\boldsymbol{\Delta}$ should be within the range of 0.40% to 0.55%. Figure 4(a) shows the loss curves of the FM for different $\boldsymbol{\Delta}$, and the $S_1(RI)$ and $S_2(T)$ at $\boldsymbol{n_a}=1.38$ and $\boldsymbol{T}=20$℃ are summarized in Fig. 4(b). Figure 4(a) indicates that as the $\boldsymbol{\Delta}$ decreases, both Peak 1 and Peak 2 shift toward longer wavelengths. This is because the refractive index of the core is proportional to $\boldsymbol{\Delta}$, and the refractive index of FM decreases. At the same time, the phase velocity increases, resulting in the RW redshift. Figure 4(b) shows that as $\boldsymbol{\Delta}$ decreases, both $S_1(RI)$ and $S_2(T)$ increase. This is because a part of the photon energy leaks from the core to the vicinity of the two Al wires when $\boldsymbol{\Delta}$ diminishes, thereby enlarging the coupling between FM and the two SPP modes. When $\boldsymbol{\Delta}=0.40\%$, both $S_1(RI)$ and $S_2(T)$ reach the

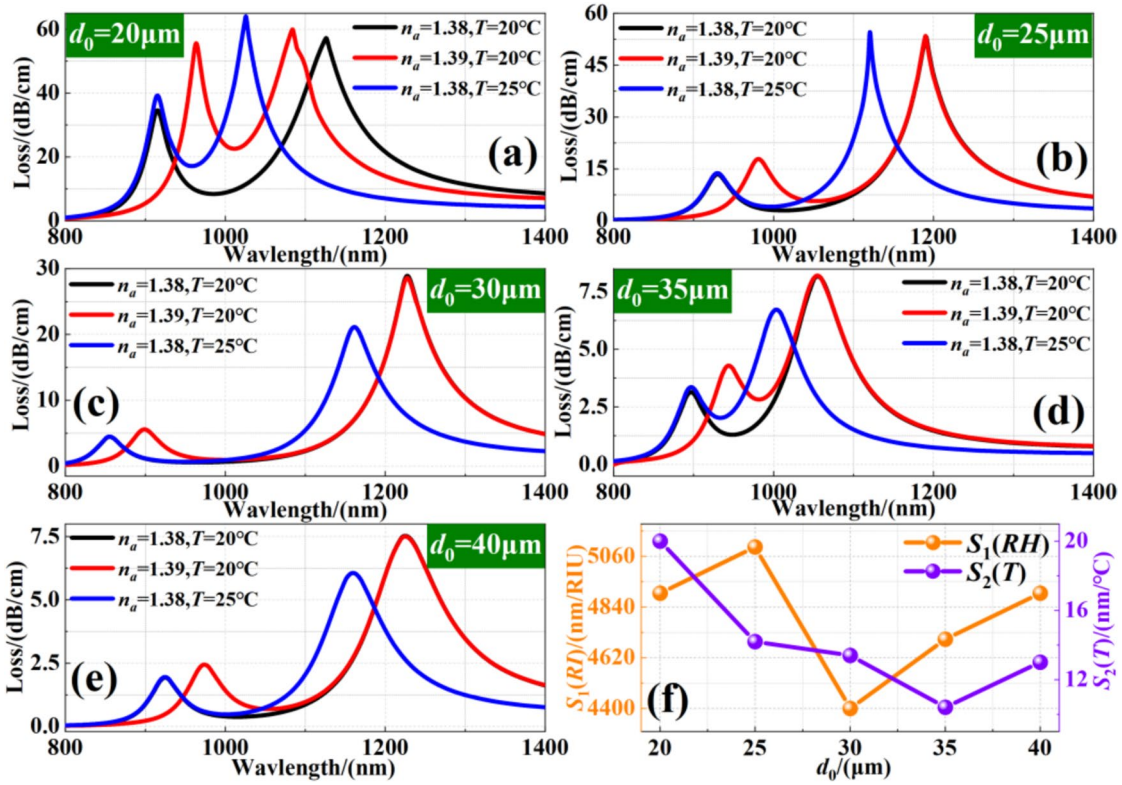

Fig. 3 (**a**-**e**) Loss curves of FM as $\boldsymbol{d_0}$ is changed from 20 μm to 40 μm; (f) $S_1(RI)$ and $S_2(T)$ of the sensor for different $\boldsymbol{d_0}$ when $\boldsymbol{n_a}=1.38$ and $\boldsymbol{T}=20$℃

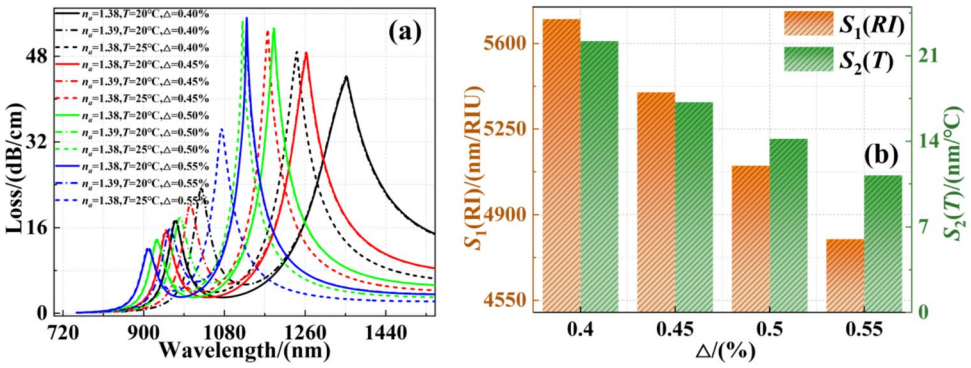

Fig. 4 (**a**) Loss spectra of FM and (**b**) Corresponding $S_1(RI)$ and $S_2(T)$ as **Δ is** changed from 0.40% to 0.55%

maximum of 5,700 nm/RIU and 22.2 nm/℃, respectively. Therefore, the **Δ** is set to 0.40%.

The Diameters of Al Wires

As the main source of the SPR effect, the diameters of the two Al wires are determined. First, $\boldsymbol{dm_1}$ is optimized between the range of 1.4 μm to 2.2 μm, and the initial parameter of $\boldsymbol{dm_1}$ is 1.0 μm. Figure 5(a) shows that as $\boldsymbol{dm_1}$ decreases, RW_{1RI} redshifts. This is because, for an Al wire with a smaller diameter, the FM energy exchange covers the entire surface of the Al wire to promote the coupling between the FM and the SPP mode [16]. At the same time, why RW_{2T} remains unaltered is that the Al wire with a diameter of $\boldsymbol{dm_1}$ mainly affects the coupling between the FM and the SPP mode of the refractive index sensing channel. Moreover, $\boldsymbol{dm_1}$ is inversely proportional to $S_1(RI)$, and $S_1(RI)$ is up to the maximum of 7,100 nm/RIU when $\boldsymbol{dm_1} = 1.4$ μm. Therefore, the $\boldsymbol{dm_1}$ is set to 1.4 μm. $\boldsymbol{dm_2}$ is adjusted based on $\boldsymbol{dm_1} = 1.4$ μm, and the original $\boldsymbol{dm_2}$ is 3.1 μm. If $\boldsymbol{dm_2}$ is increased, $S_2(T)$ decreases, so $\boldsymbol{dm_2}$ should be reduced. When $\boldsymbol{dm_2} = 2.8$ μm, $S_2(T)$ declines again, the optimization range of $\boldsymbol{dm_2}$ should be $2.8\ \mu m \le \boldsymbol{dm_2} \le 3.2\ \mu m$. Figure 5(b) presents the relationship between $S_1(RI)$ and $S_2(T)$ for different $\boldsymbol{dm_2}$. Apparently, $S_1(RI)$ remains constantly at 7,100 nm/RIU because the Al wire with a diameter of $\boldsymbol{dm_2}$ mainly affects the coupling between the FM and the SPP mode of the temperature-sensing channel. $S_2(T)$ reaches the maximum of 22.6 nm/℃ when $\boldsymbol{dm_2} = 2.9$ μm. Hence, $\boldsymbol{dm_2}$ is set to be 2.9 μm.

Distance between the Core and Al Wires

For $\boldsymbol{d_0}$, **Δ**, $\boldsymbol{dm_1}$, and $\boldsymbol{dm_2}$ equal to 25.0 μm, 0.40%, 1.4 μm, and 2.9 μm respectively, the distances between the core and two Al wires are adjusted. $\boldsymbol{L_1}$ is first optimized based on the initial $\boldsymbol{L_1}$ value of0.5 μm. When $\boldsymbol{L_1}$ is increased fro m 0.5 μm to 0.6 μm, $S_1(RI)$ decreases, so $\boldsymbol{L_1}$ should be reduced. If $\boldsymbol{L_1} < 0.2$ μm, it is not accurate enough to etch the rectangular groove by the femtosecond laser. Therefore, $\boldsymbol{L_1}$ should be adjusted within the range of 0.2 μm to 0.6 μm. Table 1 shows the relationship between $S_1(RI)$ and

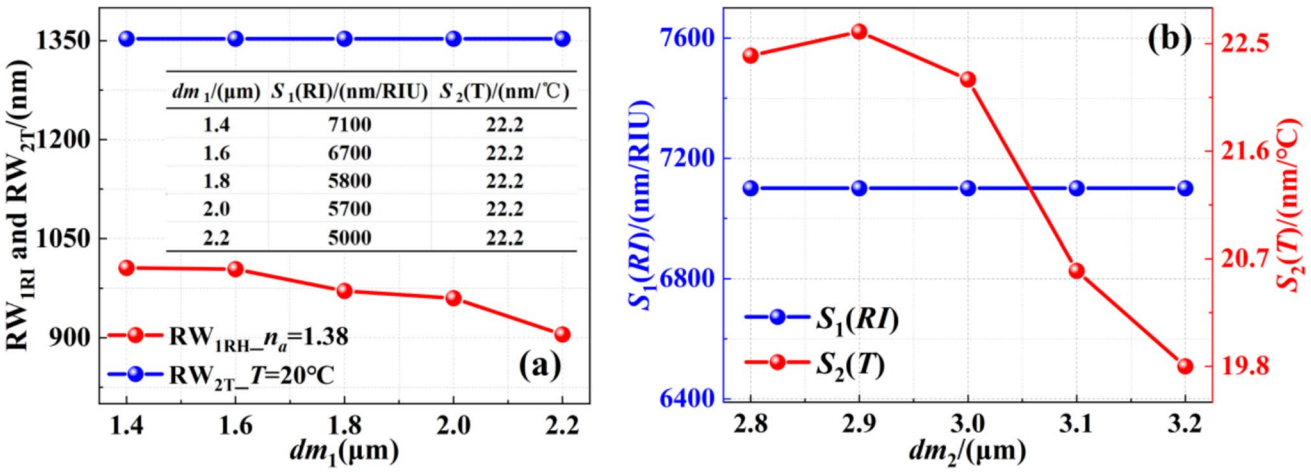

Fig. 5 (**a**) Relationship between RW_{1RI}, RW_{2T} and $\boldsymbol{dm_1}$; (**b**) Alternation of $S_1(RI)$ and $S_2(T)$ when $\boldsymbol{dm_2}$ changes from 2.8 μm to 3.2 μm

Table 1 RW_{1RI}, $S_1(RI)$, and $S_2(T)$ for different L_1

L_1/(μm)	RW_{1RI}/(nm)	$S_1(RI)$/(nm/RIU)	$S_2(T)$/(nm/℃)
0.2	1079	8400	22.6
0.3	1049	7900	22.6
0.4	1026	7500	22.6
0.5	1006	7100	22.6
0.6	989	6700	22.6

$S_2(T)$ for different $\boldsymbol{L_1}$. As the $\boldsymbol{L_1}$ increases, RW_{1RI} shifts toward shorter wavelengths. This is because the penetration depth of the evanescent wave is limited, and a larger $\boldsymbol{L_1}$ inhibits the coupling between the FM and the SPP mode. Meanwhile, the refractive index of the FM increases, and $S_1(RI)$ declines continuously. For the identical reason as $\boldsymbol{dm_1}$, $S_2(T)$ does not change with $\boldsymbol{L_1}$. As a result, when $\boldsymbol{L_1} = 0.2$ μm, $S_1(RI)$ reaches the maximum of 8,400 nm/RIU, and $\boldsymbol{L_1}$ is set to 0.2 μm.

Finally, based on $\boldsymbol{L_1} = 0.2$ μm, $\boldsymbol{L_2}$ is optimized. The initial parameter of $\boldsymbol{L_2}$ is 0.5 μm, and the optimization range is $0.3\ \mu m \le \boldsymbol{L_2} \le 0.6\ \mu m$. Table 2 indicates that as $\boldsymbol{L_2}$ increases, RW_{2T} blueshifts for the same reason as $\boldsymbol{L_1}$. At the same time, $S_2(T)$ decreases continuously, and $S_1(RI)$ is fixed for the same reason as $\boldsymbol{dm_2}$. $S_2(T)$ is the largest at 52.0 nm/℃ when $\boldsymbol{L_2} = 0.3$ μm. However, Fig. 6 shows that when $\boldsymbol{L_2} = 0.3$ μm, the FWHM of Peak 2 is too large and not conducive to sensing temperature changes accurately Therefore, $\boldsymbol{L_2}$ is set to 0.4 μm.

$\boldsymbol{R}$ and $\boldsymbol{t}$ do not affect the energy conversion between the FM and two SPP modes. Therefore, tweaking of $\boldsymbol{R}$ and $\boldsymbol{t}$ has a relatively high degree of freedom compared to other structural parameters. To facilitate fusion splicing with the MMF, $\boldsymbol{R}$ and $\boldsymbol{t}$ are 42.5 μm and 20.0 μm, respectively, thus making the diameter of the sensor to be 125 μm. In summary, after systematic optimization, the optimal structural parameters of the DCHF-based dual-parameter sensor are $\boldsymbol{d_0} = 55.0$ μm, $\boldsymbol{\Delta} = 0.40\%$, $\boldsymbol{dm_1} = 1.4$ μm, $\boldsymbol{dm_2} = 2.9$ μm, $\boldsymbol{L_1} = 0.2$ μm, $\boldsymbol{L_2} = 0.4$ μm, $\boldsymbol{R} = 42.5$ μm and $\boldsymbol{t} = 20.0$ μm. The $S_1(RI)$ and $S_2(T)$ values corresponding to these structural parameters at $\boldsymbol{n_a} = 1.38$ and $\boldsymbol{T} = 20$ ℃ are 8,400 nm/RIU and 31.2 nm/℃, which are 178.7% and 300.0% of those before optimization.

Table 2 RW_{2T}, $S_1(RI)$ and $S_2(T)$ for different L_2

L_2/(μm)	RW_{2T}/(nm)	S_1(RI)/(nm/RIU)	S_2(T)/(nm/℃)
0.3	1676	8400	52.0
0.4	1482	8400	31.2
0.5	1353	8400	22.8
0.6	1277	8400	18.8

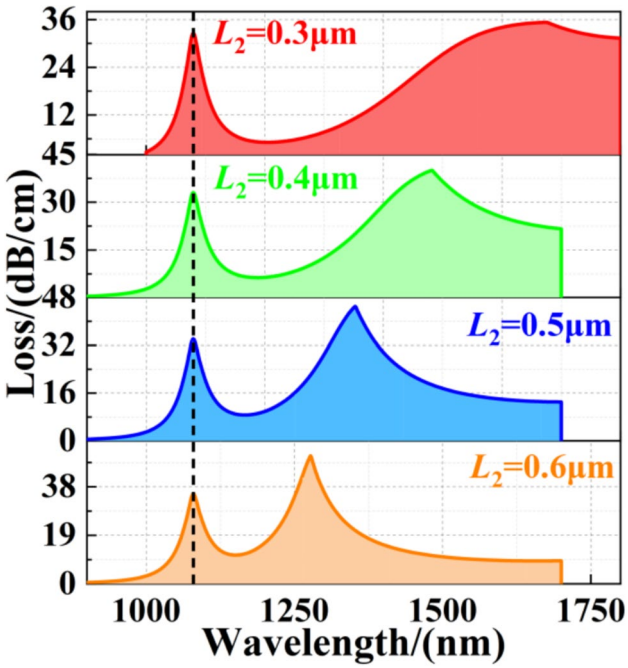

Fig. 6 Loss curves of FM for $\boldsymbol{L_2}$ equal to 0.3 μm, 0.4 μm, 0.5 μm, and 0.6 μm

Refractive Index Sensing and Temperature Sensing

When the temperature is maintained at 20 ℃, the FM loss curves for different $\boldsymbol{n_a}$ are shown in Fig. 7(a). The DCHF-based dual-parameter sensor can detect refractive indexes in the range between 1.30 and 1.39. As $\boldsymbol{n_a}$ increases, Peak 1 redshifts gradually, and the peak loss continuously increases. This is because a large portion of the photon energy is transferred from the Ge-doped core to the surface of the Al wire when $\boldsymbol{n_a}$ increases, thus reducing the refractive index of the FM. At the same time, the coupling between the FM and SPP modes increases and so does the loss of FM. Since the variation of $\boldsymbol{n_a}$ almost does not affect the refractive index of the thermo-sensitive liquid, Peak 2 hardly shifts. Figure 7(b) summarizes the $S_1(RI)$ and $S_2(RI)$ values of the sensor for different $\boldsymbol{n_a}$. Figure 7(b) shows that $S_1(RI)$ at any $\boldsymbol{n_a}$ is not less than 2,100 nm/RIU, and the highest value is 8,400 nm/RIU when $\boldsymbol{n_a} = 1.38$. $S_2(RI)$ is almost fixed compared to $S_1(RI)$, because Peak 2 is less sensitive to the change of $\boldsymbol{n_a}$ than Peak 1. The relationship between RW_{1RI} and $\boldsymbol{n_a}$, RW_{2RI} and $\boldsymbol{n_a}$ in Fig. 7(c) is obtained by linear fitting with R^2 greater than 95.3%. Furthermore, by calculating the first-order derivative of $\boldsymbol{n_a}$ from the fitted equation of RW_{1RI}, the average refractive index sensitivity is obtained to be 4,035.76 nm/RIU. Similarly, according to the fitted equations of RW_{2RI}, the average refractive index sensitivity is 63.94 nm/RIU.

When the refractive index of the analyte is 1.38, the FM loss curves at different temperatures are shown in Fig. 8(a).

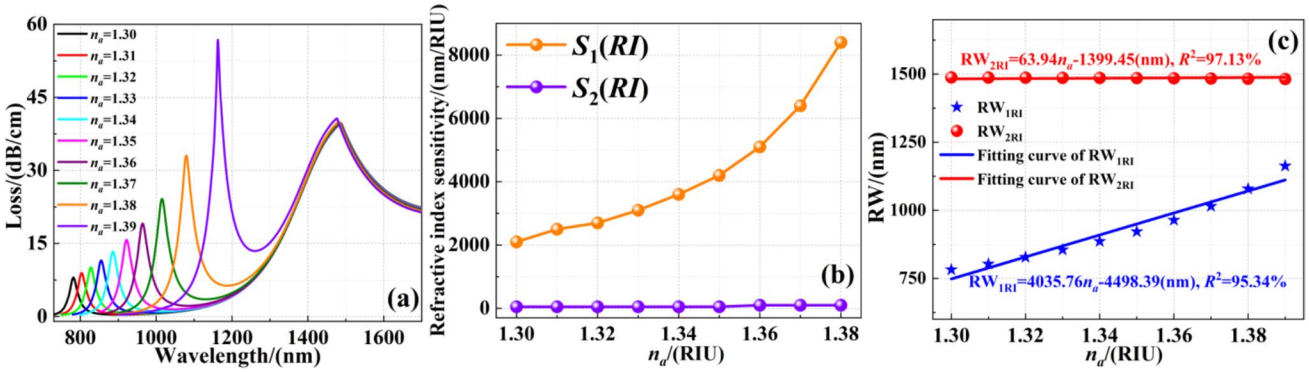

Fig. 7 (**a**) FM loss spectra and (**b**) Refractive index sensitivities of the DCHF-based dual-parameter sensor between 1.30 and 1.39; (c) Linear fitting between RW_{1RI}, RW_{2RI}, and $\boldsymbol{n_a}$

It is obvious that the DCHF-based dual-parameter sensor can detect $\boldsymbol{T}$ between 20 ℃ and 60 ℃. As $\boldsymbol{T}$ rises, Peak 2 shifts gradually toward shorter wavelengths because the refractive index of the thermo-sensitive liquid is inversely proportional to $\boldsymbol{T}$ and leads to increasing refractive indexes of FM. Figure 8(b) summarizes the $S_1(T)$ and $S_2(T)$ values at different temperatures. Figure 8(b) shows that $S_2(T)$ at any temperature is not less than 5.2 nm/℃, and $S_2(T)$ reaches the maximum of 37.6 nm/℃ when $\boldsymbol{T}=20$℃. The reason why $S_1(T)$ stays at 0 nm/℃ is that Peak 1 is insensitive to temperature. As shown in Fig. 8(c), there is a segmented linear relationship between RW_{2T} and $\boldsymbol{T}$ and RW_{1T} is constant regardless of $\boldsymbol{T}$. The fitted equations in Fig. 8(c) show that R^2 is larger than 97.2%. In addition, similar to the average refractive index sensitivity, the average temperature sensitivities are 24.48 nm/°C (20℃ ≤ $\boldsymbol{T}$ ≤ 30℃), 7.10 nm/℃ (35℃ ≤ $\boldsymbol{T}$ ≤ 60℃), and 0 nm/℃ in the temperature range between 20 °C and 60 °C.

Figure 7(c) and Fig. 8(c) reveal that Peak 1 and Peak 2 have different average refractive index sensitivities and average temperature sensitivities. RW_{1RI} and RW_{2RI} exhibit an approximately linear relationship with $\boldsymbol{n_a}$, and so do RW_{1T} and RW_{2T} with $\boldsymbol{T}$. Therefore, simultaneous detection of $\boldsymbol{n_a}$ and $\boldsymbol{T}$ can be achieved by constructing the sensitivity matrix shown in Eq. (10) [25]:

$$\begin{bmatrix} \Delta RW_1 \\ \Delta RW_2 \end{bmatrix} = \begin{bmatrix} AS_1(RI) & AS_1(T) \\ AS_2(RI) & AS_2(T) \end{bmatrix} \begin{bmatrix} \Delta n_a \\ \Delta T \end{bmatrix} \tag{10}$$

where ΔRW_1 and ΔRW_2 are the wavelength variation of the two peaks, $AS_1(RI)$ and $AS_2(RI)$ are the average refractive index sensitivities of Peak 1 and Peak 2, $AS_1(T)$ and $AS_2(T)$ are the average temperature sensitivities of Peak 1 and Peak 2, and $\Delta\boldsymbol{n_a}$ and $\Delta\boldsymbol{T}$ are the variations of the refractive index of the analyte and temperature. Besides, the measurement matrix can be inversely computed to get the sensing matrix for $\boldsymbol{n_a}$ and $\boldsymbol{T}$:

$$\begin{bmatrix} \Delta n_a \\ \Delta T \end{bmatrix} = \begin{bmatrix} AS_1(RI) & AS_1(T) \\ AS_2(RI) & AS_2(T) \end{bmatrix}^{-1} \begin{bmatrix} \Delta RW_1 \\ \Delta RW_2 \end{bmatrix} \tag{11}$$

Substituting the four average sensitivities into Eq. (11) produces Eq. (12). By monitoring the changes of Peak 1 and Peak 2 in the FM loss curves, $\boldsymbol{n_a}$ and $\boldsymbol{T}$ can be demodulated simultaneously:

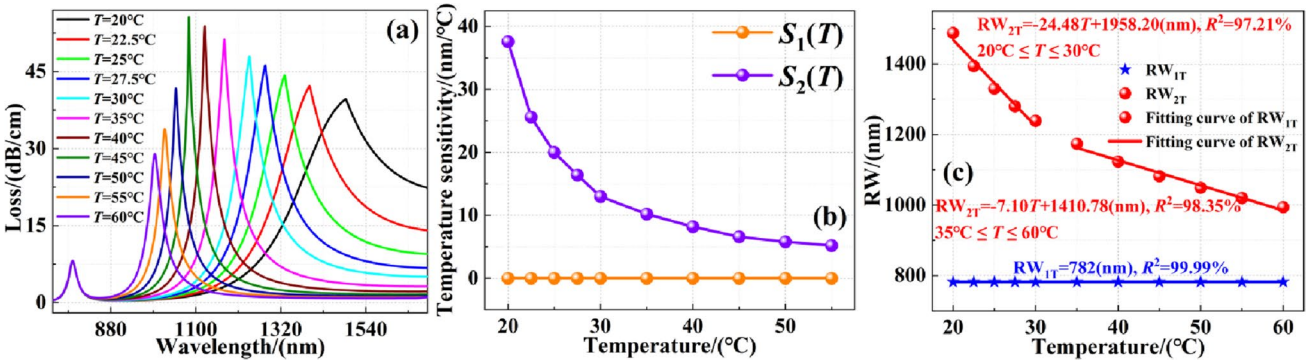

Fig. 8 (**a**) FM loss curves and (b) Temperature sensitivities of the DCHF-based dual-parameter sensor between 20 ℃ and 60 ℃; (c) Linear fitting between RW_{1T}, RW_{2T}, and $\boldsymbol{T}$

$$\begin{cases} \begin{bmatrix} \Delta n_a \\ \Delta T \end{bmatrix} = \begin{bmatrix} 2.48 \times 10^{-4} & 0 \\ 6.47 \times 10^{-4} & -4.08 \times 10^{-2} \end{bmatrix} \begin{bmatrix} \Delta RW_1 \\ \Delta RW_2 \end{bmatrix}, \begin{cases} 1.30 \le n_a \le 1.38 \\ 20°C \le T \le 30°C \end{cases} \\ \begin{bmatrix} \Delta n_a \\ \Delta T \end{bmatrix} = \begin{bmatrix} 2.48 \times 10^{-4} & 0 \\ 2.23 \times 10^{-3} & -1.41 \times 10^{-1} \end{bmatrix} \begin{bmatrix} \Delta RW_1 \\ \Delta RW_2 \end{bmatrix}, \begin{cases} 1.30 \le n_a \le 1.38 \\ 35°C \le T \le 60°C \end{cases} \end{cases} \tag{12}$$

Discussion

Manufacturing Feasibility

The DCHF-based dual-parameter sensor can be fabricated by the process illustrated in Fig. 9. Firstly, the modified chemical vapor deposition (MCVD) method is utilized to prepare the fiber preform with the corresponding dimensions. Secondly, the cleaned fiber preform is drawn into an optical fiber by a fiber drawing tower. Thirdly, a femtosecond laser is used to symmetrically etch the two rectangular channels on both sides of the optical fiber. Fourthly, a high-precision fixture is utilized to clamp the Al wire with a diameter of 1.4 μm. The position of the fixture is adjusted under a high-magnification microscope and the Al wire is introduced into one of the rectangular grooves. An ultrasonic treatment [26] produces a high-frequency microscopic displacement of the Al wire. When the Al wire moves to the position close to the core, it is fixed on the rectangular groove with a small amount of curing glue. An Al wire with a diameter of 2.9 μm is fixed on the other rectangular groove by the same method. Fifthly, the DCHF is encapsulated in a glass capillary. Both the refractive index and the inner diameter of the glass capillary match those of the cladding of the DCHF. Sixthly, the channel where the 1.4 μm Al wire is located is blocked with curing glue and inserted into the end by curing glue into a container filled with $CHCl_3$. The channel is filled with $CHCl_3$ by capillary action. The DCHF is taken out and the end is cut off with the curing agent. Afterward, a femtosecond laser is used again to etch the part of the glass tube outside the channel that is not filled with $CHCl_3$ to make it communicate with the outside. The MMFs are spliced on both sides to leave ports for subsequent detection. Finally, the analyte is placed around the sensor to complete the fabrication of the DCHF-based dual-parameter sensor. In this structure, the analyte and thermo-sensitive liquid do not affect each other during the filling process and more importantly, the sensor can be reused multiple times by rinsing with distilled water.

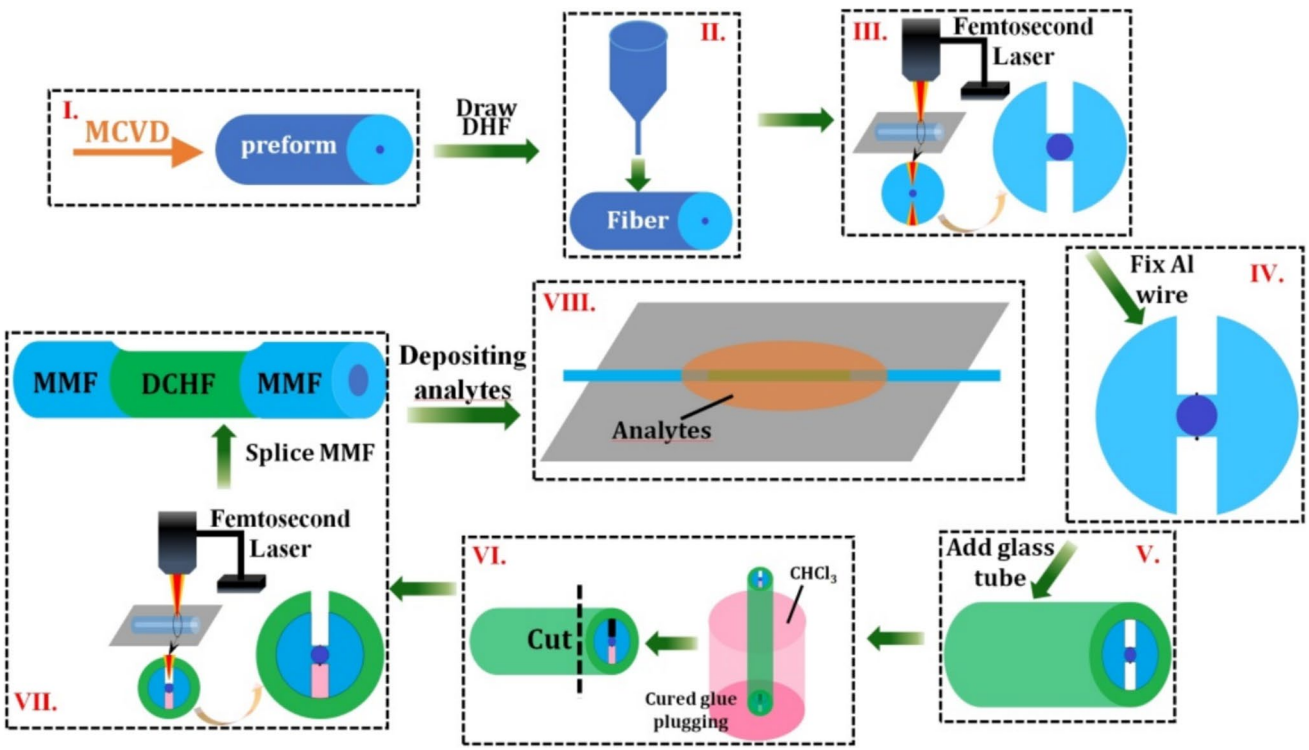

Fig. 9 Fabrication process of the DCHF-based dual-parameter sensor

Fabrication Tolerance

The fabrication tolerance refers to the allowable variation range of the structural parameters when the sensor is manufactured and is an indication of the performance stability of the sensor. As aforementioned, the characteristics of the DCHF-based dual-parameter sensor mainly depend on the Ge-doped core diameter, diameters of the two Al wires, and distances between the Al wires and the core. Table 3 summarizes the changes of $S_1(RI)$ and $S_2(T)$ when $\boldsymbol{d_0}$, $\boldsymbol{dm_1}$, $\boldsymbol{dm_2}$, $\boldsymbol{L_1}$, and $\boldsymbol{L_2}$ fluctuate within the range of ± 3%. When $\boldsymbol{d_0}$ changes ± 3%, the maximum variations of $S_1(RI)$ and $S_2(T)$ are 3.57% and 4.49% respectively. When $\boldsymbol{dm_1}$ and $\boldsymbol{L_1}$ fluctuate within the same range, the minimum variation of $S_1(RI)$ is only 0.36%. In addition, when $\boldsymbol{dm_2}$ and $\boldsymbol{L_2}$ vary ± 3%, the maximum alternation of $S_2(T)$ does not exceed 7.69%, which is still in the acceptable range. In summary, the DCHF-based dual-parameter sensor has high manufacturing tolerance and practicality.

Table 3 $S_1(RI)$ and $S_2(T)$ when some parameters vary within the range of ± 3%

Parameters	Tolerance	$S_1(RI)$	$S_2(T)$
$\boldsymbol{d_0}$	−3%	8100 nm/RIU	32.2 nm/℃
	0	8400 nm/RIU	31.2 nm/℃
	+3%	8600 nm/RIU	29.8 nm/℃
$\boldsymbol{dm_1}$	−3%	8450 nm/RIU	**N/A**
	0	8400 nm/RIU	
	+3%	8370 nm/RIU	
$\boldsymbol{dm_2}$	−3%	**N/A**	31.2 nm/℃
	0		31.2 nm/℃
	+3%		31.2 nm/℃
$\boldsymbol{L_1}$	−3%	8500 nm/RIU	**N/A**
	0	8400 nm/RIU	
	+3%	8300 nm/RIU	
$\boldsymbol{L_2}$	−3%	**N/A**	32.6 nm/℃
	0		31.2 nm/℃
	+3%		28.8 nm/℃

Comparison of Properties

In order to highlight the advantages of the DCHF-based dual-parameter sensor, Table 4 compares the properties of our sensor with those of similar devices in the literature in terms of the refractive index detection range, maximum refractive index sensitivity, temperature detection range, and maximum temperature sensitivity. The refractive index detection range and temperature detection range of our sensor are in line with those described in Refs. [12–14, 27], but the maximum refractive index sensitivity is improved significantly. In fact, the maximum temperature sensitivity increases by more than one order of magnitude compared to that in Refs. [12–14, 27]. Most importantly, it is easy to fill the DCHF-based dual-parameter sensor with the analyte and thermo-sensitive liquid, and the two do not affect each other.

Table 4 Comparison of dual-parameter sensors for refractive index and temperature sensing

Refs.	Refractive index range	Max Refractive index sensitivity	Temperature range	Max temperature sensitivity	Cross-section
[12]	1.35-1.46	5000 nm/RIU	20-50°	3.00 nm/°	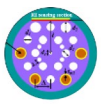
[13]	1.35-1.40	3940 nm/RIU	20-60°	1.08 nm/°	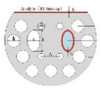
[14]	1.35-1.40	4520 nm/RIU	20-60°	4.83 nm/°	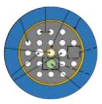
[27]	1.33-1.36	2214 nm/RIU	20-60°	1.81 nm/°	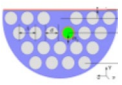
This work	***1.30-1.39***	***8400 nm/RIU***	***20-60°***	***37.6 nm/°***	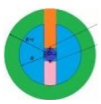

Conclusion

A DCHF-based dual-parameter sensor is designed for the simultaneous detection of the analyte refractive index and temperature. The sensor contains symmetrical rectangular grooves on both sides of the Ge-doped core formed by a femtosecond laser inlaid into a notched capillary. The thermo-sensitive liquid is placed in the closed channel to detect temperature, while the analyte is filled in the channel near the notch to detect the refractive index. To improve the refractive index sensitivity and temperature sensitivity, Al wires with different diameters are placed close to the core in the two rectangular grooves to excite SPR. With $S_1(RI)$ and $S_2(T)$ as the main optimization benchmarks, a systematic and comprehensive optimization of the structural parameters of the sensor is carried out. The optimal structural parameters are $\boldsymbol{d_0}=55.0$ μm, $\boldsymbol{\Delta}=0.40\%$, $\boldsymbol{dm_1}=1.4$ μm, $\boldsymbol{dm_2}=2.9$ μm, $\boldsymbol{L_1}=0.2$ μm, $\boldsymbol{L_2}=0.4$ μm, $\boldsymbol{R}=42.5$ μm, and $\boldsymbol{t}=20.0$ μm. Numerical analysis shows that the DCHF-based dual-parameter sensor can simultaneously detect refractive indexes in the range between 13.0 and 1.39 and temperature between 20 ℃ and 60 ℃. The maximum refractive index sensitivity of 8,400 nm/RIU is much better than that of previously reported devices, while the maximum temperature sensitivity of 37.6 nm/℃ is more than one order of magnitude higher. Assessment of the fabrication tolerance indicates a good ability to compensate for manufacturing errors. In summary, the DCHF-based dual-parameter sensor boasts high sensitivity, easy filling of the analyte and thermo-sensitive liquid without mutual influence, and high integration, thereby boding well for a variety of applications such as chemical analysis and environmental monitoring.

Author Contribution Zhenshi Chen provided the innovation points of this article, conducted simulation work using COMSOL, and also wrote the article. Chengkun Yang is the corresponding author of this article. Haihao Fu drew all the curve graphs, schematic diagrams and structure diagrams in the article. Paul. K. Chu improved the English quality of the article.

Funding This work was funded by National Natural Science Foundation of China (NSFC), grant number 62205383.

Data Availability No datasets were generated or analysed during the current study.

Declarations

Conflict of interest The authors declare no competing interests.

References

1. Singh S (2002) Refractive index measurement and its applications. Phys Scr 65(2):167–180
2. Teng C, Min R, Zheng J, Deng S, Li M, Hou L, Yuan L (2021) Intensity-modulated polymer optical fiber-based refractive index sensor: a review. Sensors 22(1):81
3. Peng C, Yang C, Zhao H, Liang L, Zheng C, Chen C, Qin L, Tang H (2023) Optical waveguide refractive index sensor for biochemical sensing. Appl Sci 13(6):3829
4. Song N, Xu X, Zhang Z, Gao F, Wang X (2023) advanced interferometric fiber optic gyroscope for inertial sensing: a review. J Lightwave Technol 41(13):4023–4034
5. Datta A, Saha A (2021) Manifestation of a highly sensitive evanescent wave absorption-based refractive index sensor realized by radiating with an optical Airy beam. Opt Quant Electron 53:1–17
6. Wang Q, Ren ZH, Zhao WM, Wang L, Yan X, Zhu A, Qiu F, Zhang KK (2021) Research advances on surface plasmon resonance biosensors. Nanoscale 14(3):564–591
7. Lv J, Wang J, Yang L, Liu W, Fu H, Chu PK, Liu C (2024) Recent advances of optical fiber biosensors based on surface plasmon resonance: sensing principles, structures, and prospects. Sens Diagn 3:1369–1391
8. Guo K, He J, Li H, Xu B, Lu S, Liu S, Xu X, Xu G, Wang Y (2022) High-spatial-resolution high-temperature sensor based on ultra-short fiber bragg gratings with dual-wavelength differential detection. J Lightwave Technol 40(7):2166–2172
9. Yin Z, Jing X, Feng Y, Gao Z, Wu B, Wang C (2022) Refractive index and temperature dual parameter sensor based on a twin-core photonic crystal fiber. J Phys D Appl Phys 55(15):155108
10. Wang J, Lu X, Mi C, Yin Q, Lv J, Yang L, Liu W, Yi Z, Liu Q, Chu PK, Liu C (2024) Ultra-high sensitivity photonic crystal fiber sensor based on dispersion turning point sensitization of surface plasmonic polariton modes for low RI liquid detection. Opt Express 32(19):32895–32908
11. Wang D, Yi Z, Ma G, Dai B, Yang J, Zhang J, Yu Y, Liu C, Wu X, Bian Q (2022) Two-channel photonic crystal fiber based on surface plasmon resonance for magnetic field and temperature dual-parameter sensing. Phys Chem Chem Phys 24(35):21233–21241
12. Danlard I, Akowuah EK (2021) Design and theoretical analysis of a dual-polarized quasi D-shaped plasmonic PCF microsensor for back-to-back measurement of refractive index and temperature. IEEE Sens J 21(8):9860–9868
13. Chen A, Yu Z, Dai B, Li Y (2021) Highly sensitive detection of refractive index and temperature based on liquid-filled D-shape PCF. IEEE Photonics Technol Lett 33(11):529–532
14. Zhang J, Yuan J, Qu Y, Qiu S, Mei C, Zhou X, Yan B, Wu Q, Wang K, Sang X, Yu C (2022) A surface plasmon resonance-based photonic crystal fiber sensor for simultaneously measuring the refractive index and temperature. Polymers 14(18):3893
15. Liu C, Lv J, Liu W, Wang F, Chu PK (2021) Overview of refractive index sensors comprising photonic crystal fibers based on the surface plasmon resonance effect [Invited]. Chin Opt Lett 19(10):102202
16. Fu H, Guo Y, Gao W, Lou S, Chu PK, Sheng Z (2024) Ultra-high sensitivity weak magnetic field detecting magnetic fluid surface plasmon resonance sensor based on a single-hole fiber. Opt Express 32(9):15025–15040
17. Luan N, Wang R, Lv W, Lu Y, Yao J (2014) Surface plasmon resonance temperature sensor based on photonic crystal fibers randomly filled with silver nanowires. Sensors 14(9):16035–16045
18. Wang Q, Zhang X, Yan X, Wang F, Cheng T (2021) Design of a surface plasmon resonance temperature sensor with multi-wavebands based on conjoined-tubular anti-resonance fiber. Photonics 8(6):231
19. Kedenburg S, Vieweg M, Gissibl T, Giessen H (2012) Linear refractive index and absorption measurements of nonlinear optical liquids in the visible and near-infrared spectral region. Optical Mater Express 2(11):1588–1611

20. Sharma AK, Gupta BD (2005) On the sensitivity and signal to noise ratio of a step-index fiber optic surface plasmon resonance sensor with bimetallic layers. Optics Communications 245(1–6):159–169
21. Milosevic M (2013) On the nature of the evanescent wave. Appl Spectrosc 67:126–131
22. Liu Y, Li S, Chen H, Li J, Zhang W, Wang M (2020) Surface plasmon resonance induced high sensitivity temperature and refractive index sensor based on evanescent field enhanced photonic crystal fiber. J Lightwave Technol 38(4):919–928
23. Xu L, Liu C, Fu H, Wang J, Li X, Lv J, Yang L, Chu PK (2022) Orbital angular momentum-excited surface plasmon resonance for liquid refractive index sensing by photonic crystal fiber with high sensitivity and wide detection range. Opt Eng 61(9):096101
24. Fu H, Sheng Z, Gao W, Guo Y, Wang B, Wang X, Lou S (2024) Ultra-high sensitive dual-parameter sensor based on double-hole fiber for simultaneous detection of magnetic field and temperature. Opt Express 32(11):20175–20193
25. Fu J, Pu S, Hao Z, Zhang C, Liu W, Duan S, Han S (2024) Reflective magnetic field and temperature dual-parameter sensor based on no-core fiber probe. Opt Laser Technol 174:110550
26. Liu S, Shan X, Guo K, Yang Y, Xie T (2018) Experimental study on titanium wire drawing with ultrasonic vibration. Ultrasonics 83:60–67
27. Yang X, Lu Y, Liu B, Yao J (2017) Simultaneous measurement of refractive index and temperature based on SPR in D-shaped MOF. Appl Opt 56(15):4369–4374